Applied Ocean Research 120 (2022) 102998

Contents lists available at ScienceDirect

Applied Ocean Research

journal homepage: www.elsevier.com/locate/apor

Application of a lumping method for fatigue design of monopile-based wind turbines using fully coupled and simplified models

George Katsikogiannis [a,*], John Marius Hegseth [b], Erin E. Bachynski-Polić [a]

[a] Department of Marine Technology, Norwegian University of Science and Technology, Trondheim NO-7491, Norway
[b] Dr.techn. Olav Olsen AS, Pirsenteret, Havnegata 9, Trondheim NO-7010, Norway

ARTICLE INFO

Keywords:
Offshore wind turbines
Fatigue design
Environmental lumping
Aero-hydro-servo-elastic
Frequency domain
Damage-equivalent contour lines

ABSTRACT

The study presents different methods for fatigue assessment of monopile-based offshore wind turbines. Their accuracy and computational time is compared to full long-term time domain results. The damage-equivalent lumping method from Katsikogiannis et al. (2021) is further examined using nonlinear fully coupled time domain models as well as simplified, frequency domain, state–space models for three turbines (5 MW, 10 MW, 15 MW). The different dynamic characteristics of these turbines affect the resultant contour lines and lumped load cases for various wave conditions. The lumping method using fully coupled models had an accuracy of 92%–98% for the total fatigue damage along the support structure for all turbines, and decreased the computational time by 90%. The simplified models were able to accurately capture the dynamic characteristics of the turbines in the lumping process, resulting in similar lumped load cases and accuracy, with further reduction of the computational effort (96%). Long-term fatigue assessment in frequency domain generally resulted in discrepancies compared to time domain assessment (40%–80%), mainly due to the linear soil stiffness, sensitivity to damping (especially for parked conditions), and the simplified representation of the control system in the simplified models. Using the simplified models to select the lumped load cases, combined with time domain analyses of the lumped cases, resulted in the best combination of accuracy and computational effort.

1. Introduction

Fatigue damage is one of the governing design factors for the foundations of offshore wind turbines (OWTs). Different methods have been developed for fatigue assessment of offshore structures, such as deterministic methods, spectral-based approaches, and time domain methods (ABS, 2014; DNV-GL, 2020). Monopile-based OWTs are highly dynamic structures subjected to simultaneous hydrodynamic and aerodynamic loads, soil–structure interaction, and control system effects. Therefore, fully integrated time-domain simulations combined with rainflow counting technique (Matsuishi and Endo, 1968) are considered the most accurate method to calculate fatigue damage, as nonlinear effects and coupling between environmental loads and structural responses can be taken into account. However, fully coupled dynamic analyses are computationally demanding, as all relevant combinations of environmental parameters within the wave scatter diagrams shall be considered.

One approach to improve the efficiency of time-domain method is to reduce the number of conditions considered for fatigue assessment, known as environmental lumping. A common practice is to lump the sea states within a wave scatter diagram into a smaller number of blocks, and representative sea states within the blocks are adopted to replace original sea states in fatigue assessment (Song et al., 2016). The main challenge of this method is to define the sea state characteristics (significant wave height, peak period, probability of occurrence) for each block that will result in accurate damage estimates (Song et al., 2016). Different approaches for selecting the representative sea states have been developed and evaluated for various offshore structures (mooring and riser systems Sheehan et al., 2005; Low and Cheung, 2012, fish cages Du et al., 2014; Hou et al., 2019, OWTs Kühn, 2001; Seidel, 2014a,b; Passon and Branner, 2014; Passon, 2015, fixed and floating platforms Song et al., 2016; Song and Wang, 2019; Jia, 2008). DNV-RP-F204 (DNV-GL, 2017b) and Sheehan et al. (2005) proposed a conservative approach to select the representative sea states, ignoring the probability of occurrence of sea states in the scatter diagram, resulting in significant overestimation of fatigue damage. Kühn (2001) and Mittendorf (2009) lumped the original sea states with same wave height into a block and the representative wave period is determined based on the probabilistic average of wave frequencies or periods,

* Corresponding author.
E-mail addresses: george.katsikogiannis@ntnu.no (G. Katsikogiannis), jmh@olavolsen.no (J.M. Hegseth), erin.bachynski@ntnu.no (E.E. Bachynski-Polić).

https://doi.org/10.1016/j.apor.2021.102998
Received 13 August 2021; Received in revised form 8 November 2021; Accepted 28 November 2021
Available online 13 January 2022

respectively. Following a similar approach, Burton et al. (2011) lumped the sea states with same wave period, and the associated wave height was determined based on a correlation between the sea state's probability of occurrence, wave height, and the m^{th} power of the wave height, where m corresponds to the S–N fatigue curve slope. Jia (2008) employed a combination of Burton's and Mittendorf's methods to calculate wave induced damage on jacket structures, however its applicability to two-segment S–N curve is still questionable. Song et al. (2016) proposed a lumping block method based on spectral moments equivalence between the representative and the original sea states, which was further developed (Song and Wang, 2019) to account for fatigue equivalence, with significant advantages compared to conventional block methods. Hou et al. (2019) proposed an improved lumping block method through selecting a more severe significant wave period and compared it with other block lumping methods for a mooring system of a fish cage.

Seidel (2014a,b) introduced an approach where the lumped sea state parameters are based on quasi-static considerations and an equivalent spectral energy that represents the entire scatter diagram, determined from the weighted spectral values of the original sea states at the first natural frequency. Passon and Branner (2014), Passon (2015) developed a damage-equivalent contour lines approach, where the sea state parameters of the lumped load cases are defined based on equivalence of a pseudo fatigue damage matrix over wave height/period that is established by means of spectral or time domain approach. His lumping method resulted in more accurate preservation of fatigue damage for different locations along the support structure, compared to Seidel's and Kühn's methods (Passon, 2015). Low and Cheung (2012) proposed a lumping method by establishing a fatigue damage function over sea state parameters for the long-term fatigue assessment of mooring and riser systems. The method was further simplified and evaluated by Du et al. (2014).

The challenge in the lumping process is to select a reduced set of load cases that captures the OWT dynamics, and can accurately predict the damage along the support structure over its lifetime. Most of the methods described above do not consider the effect of wind, which is crucial for the OWT operation (e.g. aerodynamic damping, soil–structure interaction) and resultant responses, others do not consider the dynamic characteristics of the structure, are sensitive to block partitioning, or result in significant overestimation of fatigue damage. Furthermore, design standards (IEC, 2019; DNV-GL, 2016b) do not provide clear recommendations for how lumping should be performed for OWTs, and application of lumping in more computationally efficient, simplified models – if these are sufficiently accurate – needs to be investigated.

Katsikogiannis et al. (2021) extended Passon's method by extracting stress transfer functions from 3-hr time domain simulations considering white-noise wave excitation and uniform wind, for each wave scatter diagram associated with a wind class. Damage estimates obtained from the stress transfer functions were used to define the damage-equivalent contour lines for different locations along the support structure, and their intersection is considered the lumped sea state representative for a wave scatter diagram. The method was applied to a 10 MW monopile-based OWT, resulting in accurate damage estimates (94%–98%) throughout the support structure, with considerable reduction of computational effort (93%).

In the present work, the damage-equivalent lumping method is further examined. The method is applied to three fully coupled monopile-based OWTs, the NREL 5 MW, the DTU 10 MW, and the IEA 15 MW. The resultant contour lines and lumped load cases are compared among the models in relation to their dynamic characteristics and wave conditions. The fatigue damage from the lumped load cases is calculated, and its accuracy is evaluated compared to full long-term fatigue assessment. The lumping method is also applied using simplified (linearized) state–space representations of the OWT models. It is shown that the method is applicable using the simplified models presented in the study, resulting in similar contour lines, and lumped load cases, as the ones obtained from the fully coupled models. The application of the lumping method using simplified models during early design can further reduce the computational time, something that can be highly beneficial, e.g. in case of design changes. Then, fully coupled time domain models can be used to analyse the lumped load cases to calculate long-term fatigue estimates. Finally, the applicability of the simplified model for full long-term fatigue assessment is also assessed, but found to provide insufficient accuracy.

The paper is organized as follows: Section 2 summarizes the environmental conditions, the fully coupled and simplified OWT simulation models, and load models considered in the study. Section 3 gives a detailed description of the damage-equivalent lumping method for the derivation of the lumped load cases. Section 4 describes the methods used in the study to calculate and compare the long-term fatigue damage. Finally, Section 5 summarizes the results and Section 6 concludes the paper with recommendations for future work.

2. Environmental conditions and simulation models

This section describes the model used in the case study, including environmental conditions, simulation models and numerical modelling approaches.

2.1. Organization of metocean data

Design of OWTs is usually based on load calculations considering simultaneous wind and wave conditions, obtained from numerical hindcast models or measurements. The Norwegian Reanalysis Archive (NORA10) (Reistad et al., 2011; Aarnes et al., 2012) hindcast data have been used here. The NORA10 hindcast is a regional dataset of 3-h resolution for the northeast Atlantic, developed by the Norwegian Meteorological Institute (Bruserud and Haver, 2016). The period from 1957 to 2017 is considered for a site at the Norwegian Continental Shelf (55.11°N, 3.47°E) with 30 m water depth. The dataset provides information about metocean parameters such as mean wind speed 10 m above sea water level (SWL), significant wave height (H_s), wave peak period (T_p), and wind-wave directionality (not considered in the study).

Metocean data used for the design are represented by wind speed-dependent scatter diagrams, which contain the probability of occurrence, $p_{k,i,j}$ for wind class k, wave height class i and peak period class j. Each wind class $k = 1, \ldots, N_{U_w}$ is associated with the mean wind speed at hub height, $U_{w,k}$. The associated wave scatter diagram, SD_k, consists of N_{H_s} classes for significant wave height and N_{T_p} classes for peak period. In the present study, wind speed classes with step of 2 m/s have been considered, including eleven operational (4–26 m/s) and two parked (26–30 m/s) classes. The sea states within each scatter diagram are gathered in H_s classes of 0.5 m and T_p classes of 1 s. The class size for each metocean parameter is taken based on recommendations of relevant design standards (IEC, 2019; DNV-GL, 2017a). Each sea state class in the wave scatter diagrams is represented by the class midpoints $H_{s,i} - T_{p,j}$. Fig. 1 shows an example of how the sea states are organized in a wave scatter diagram associated with a wind class.

2.2. OWT simulation models

Three monopile-based OWT models were used in the study: the NREL 5 MW (Jonkman et al., 2009), the DTU 10 MW (Bak et al., 2013) and the IEA 15 MW (Gaertner et al., 2020). Their main characteristics are shown in Table 1. The lumping method was applied using two representations of the OWT models. In the first, the OWTs were represented by fully coupled nonlinear time domain models (Section 2.2.1), while in the second, the wind turbine systems were fully linearized and represented by simplified frequency domain state–space models (Section 2.2.2). Fig. 2 shows a simplified illustration of the OWTs.

	Tp class	[3-4]	[4-5]	[5-6]	[6-7]	[7-8]	[8-9]	[9-10]	[10-11]	[11-12]	[12-13]	[13-14]	[14-15]	[15-16]	[16-17]	[17-18]	[18-19]
	Tp,j [s]	3,5	4,5	5,5	6,5	7,5	8,5	9,5	10,5	11,5	12,5	13,5	14,5	15,5	16,5	17,5	18,5
Hs class	Hs,i [m]																
[0-0.5]	0,25																
[0.5-1.0]	0,75																
[1.0-1.5]	1,25		1,69E-05	2,81E-05	5,62E-06	5,62E-06	1,12E-05										
[1.5-2.0]	1,75			2,02E-04	8,26E-04	8,99E-05	1,69E-05	2,25E-05	2,25E-05	2,81E-05	3,37E-05	5,62E-06	5,62E-06				
[2.0-2.5]	2,25			2,25E-05	1,55E-03	5,39E-03	1,01E-03	4,49E-05	5,62E-06	3,93E-05	1,12E-05	1,12E-05	5,62E-06				
[2.5-3.0]	2,75				7,87E-05	6,05E-03	1,22E-02	8,65E-04	7,30E-05	2,25E-05	3,93E-05	2,81E-05	1,69E-05	5,62E-06			
[3.0-3.5]	3,25					2,92E-04	7,52E-03	9,11E-03	1,43E-03	2,47E-04	7,30E-05	2,25E-05	3,37E-05	1,12E-05			
[3.5-4.0]	3,75					1,69E-05	1,63E-04	2,72E-03	2,76E-03	1,19E-03	3,26E-04	6,74E-05	2,81E-05	5,62E-06	1,69E-05		
[4.0-4.5]	4,25							9,55E-05	4,44E-04	7,92E-04	7,42E-04	2,13E-04	3,37E-05	1,12E-05	1,12E-05	5,62E-06	
[4.5-5.0]	4,75								2,25E-05	8,99E-05	1,74E-04	1,85E-04	6,18E-05	2,25E-05	2,25E-05	5,62E-06	
[5.0-5.5]	5,25									5,62E-06	5,62E-06	3,93E-05	2,25E-05	5,62E-06			
[5.5-6.0]	5,75														5,62E-06	5,62E-06	
[6.0-6.5]	6,25													1,12E-05			
[6.5-7.0]	6,75																

Fig. 1. Organization of sea state parameters in a wave scatter diagram SD_k associated with wind class k where $U_{w,k} \in [U_l, U_h]$, with U_l, U_h representing the lower, and upper bounds of the wind class k, respectively. Each class in SD_k contains the probability of occurrence for each sea state, $p(H_{s,i}, T_{p,j} | U_{w,k} \in [U_l, U_h])$.

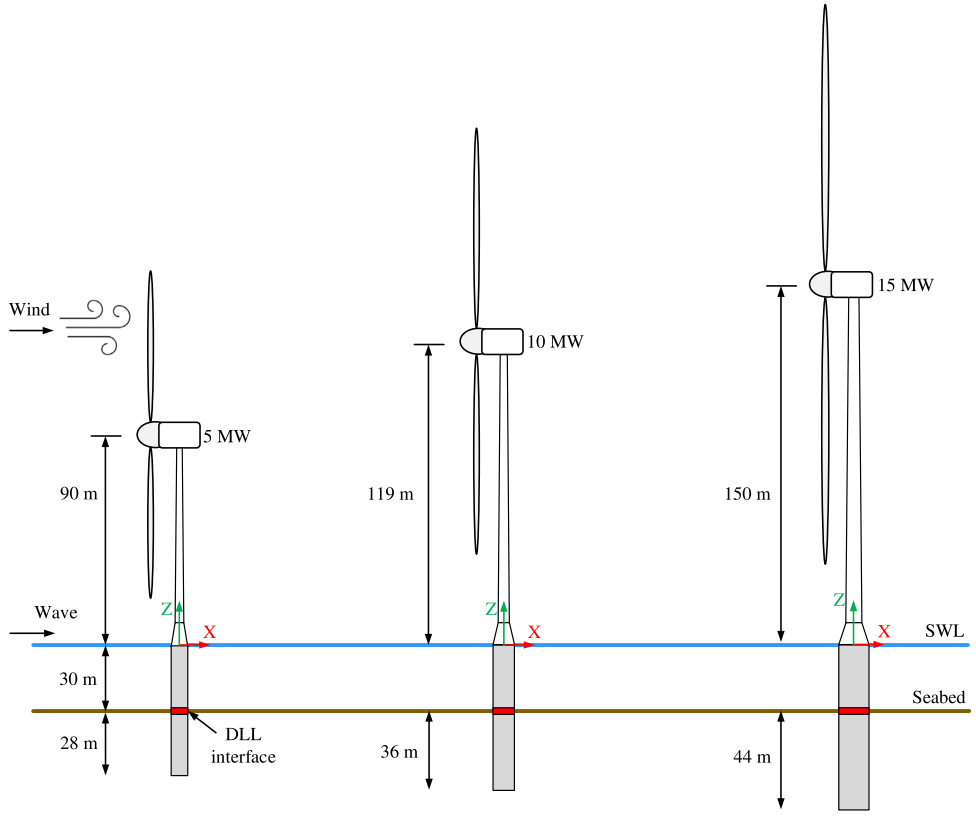

Fig. 2. Illustration of the three OWT models.

Table 1
Main characteristics of the three monopile-based OWT models used in the study.

Parameter	Unit	NREL	DTU	IEA
Rated power	MW	5	10	15
Rated wind speed	m/s	11.4	11.4	10.59
Rated rotor speed	rpm	12.1	9.6	7.56
Hub height	m	90	119	150
Rotor diameter	m	126	178.3	240
Rotor-nacelle assembly mass	tonnes	350	674	1017
Monopile diameter	m	7	9	11
Monopile wall thickness	m	0.07	0.11	0.11
Embedded length	m	28	36	44

2.2.1. Fully coupled time domain models

For the fully coupled, nonlinear, time domain models the rotor-nacelle assembly (RNA), tower and monopile above seabed were modelled in the aero-hydro-servo-elastic simulation tool SIMA (SIMO, 2017; RIFLEX, 2017). Structural components of the support structure were modelled as axisymmetric beam elements. The monopile has a constant diameter and wall thickness along its length, while the tower consists of sections of constant diameter and wall thickness, decreasing from the tower base to the tower top. The wind turbine blades, and control systems were modelled based on publicly available reference turbines (Jonkman et al., 2009; Bak et al., 2013; Gaertner et al., 2020).

For the OWT foundations (monopile below mudline), a non-linear macro-element model formulated using elasto-plasticity theory was used, where the foundation and surrounding soil are condensed to a force–displacement relation at mudline (Correia, 2011). The macro-element model includes the contribution of soil resistance components

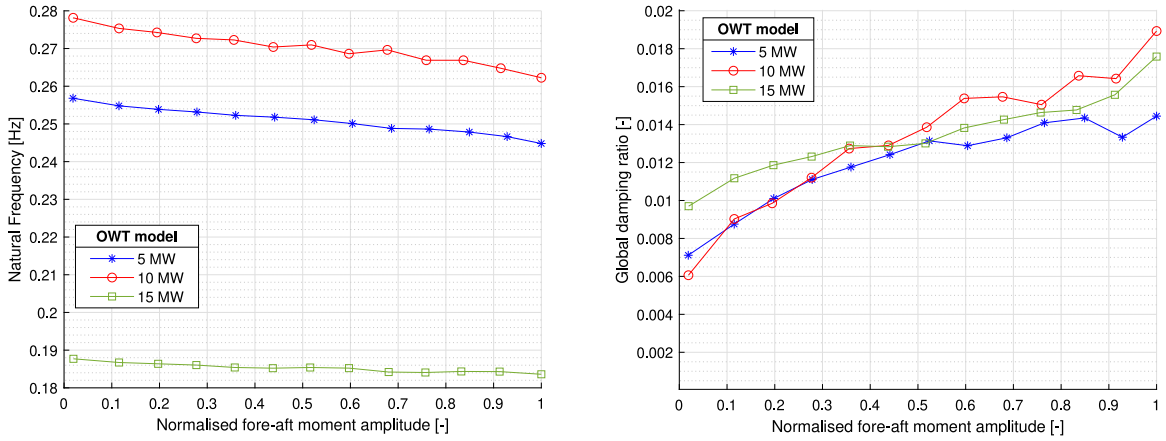

(a) Natural frequencies **(b)** Global damping ratios

Fig. 3. Dynamic properties of the OWT models from the free-vibration test (parked and feathered rotor).

such as base and side shear, and it is able to reproduce the non-linear load–displacement response and the hysteretic damping effects of monopile-based OWTs in integrated time domain simulations (Page et al., 2017, 2018, 2019). The macro-element model used in this study is calibrated to FEA results of full 3D continuum modelling of the soil volume and the foundation. Details of the soil layer properties used for the macro-element model calibration were given by Katsikogiannis et al. (2021). The model communicates with SIMA through a dynamic link library (DLL). The macro-element model does not directly compute the forces along the monopile below seabed, therefore a separate post-processing numerical tool has been employed for that purpose.

The dynamic properties of the three OWT models were found from a free decay test with no wind and no waves. The maximum thrust force for each model was gradually applied at the tower top and then released to allow the OWT to vibrate. Aerodynamic damping was negligible during the decay test as the rotor was kept locked and the blades were pitched to 90°. Fig. 3 shows the first natural frequency and global damping ratio as quantified from the time history of the fore-aft bending moment at the mudline using the logarithmic decrement method (Katsikogiannis et al., 2021). The response amplitude (x-axis) is normalized by the thrust force at rated wind speed multiplied by the distance from hub height to seabed.

For the time domain simulations, the incoming wind field was generated using the stochastic, full-field, turbulence simulator TurbSim from NREL (Jonkman, 2009). The Kaimal spectrum and exponential coherence model (IEC, 2019) were used. Aerodynamic loads were calculated using the blade element momentum theory, including the Glauert correction, Prandtl corrections for tip loss and hub loss (Burton et al., 2011), and dynamic stall and dynamic wake (Bachynski and Ormberg, 2015).

Two wave kinematic theories have been used in the study: Airy linear wave theory and Stokes' 2nd order waves. The transition between the two theories was selected by comparing the wave loads on a rigid monopile. It was found that Airy theory with constant potential up to the instantaneous undisturbed surface elevation was sufficient for $H_s \leq$4.5 m. Morison's equation and the MacCamy & Fuchs formulation (MacCamy R.C., 1954) (to account for diffraction effects) with Morison type drag have been used for wave load modelling. The drag (C_D) and inertia (C_M) coefficients were assumed to be 0.9 and 2.0, respectively (DNV-GL, 2017a) for Morison's equation. The added mass coefficient is assumed to be constant and equal to 1.0 for the MacCamy & Fuchs hydrodynamic model. Table 2 summarizes the load formulation and wave kinematics theories in the study.

Table 2
Overview of load formulation and wave kinematics in time domain model.

	$T_p \leq 10$ s	$T_p > 10$ s
$H_s \leq 4.5$ m	MacCamy & Fuchs/Airy theory	Morison/Airy theory
$H_s > 4.5$ m	MacCamy & Fuchs/Airy theory	Morison/2nd order waves

2.2.2. Simplified response model

For the simplified OWT models, a linear representation of the wind turbine system was created (Fig. 4). The support structure was modelled as a slender beam undergoing pure bending deformations, and was assumed to follow Euler–Bernoulli beam theory. The RNA was assumed rigid, and thus replaced by a point mass and inertia at the tower top. The soil was replaced by a linear stiffness matrix at the mudline, which represents the linear stiffness of the macro-element models that were used in the fully coupled models. Structural, soil, and hydrodynamic damping were described using stiffness-proportional Rayleigh damping along the support structure. The Rayleigh damping for each OWT model was tuned so the global damping ratio is approximately 1.3%.

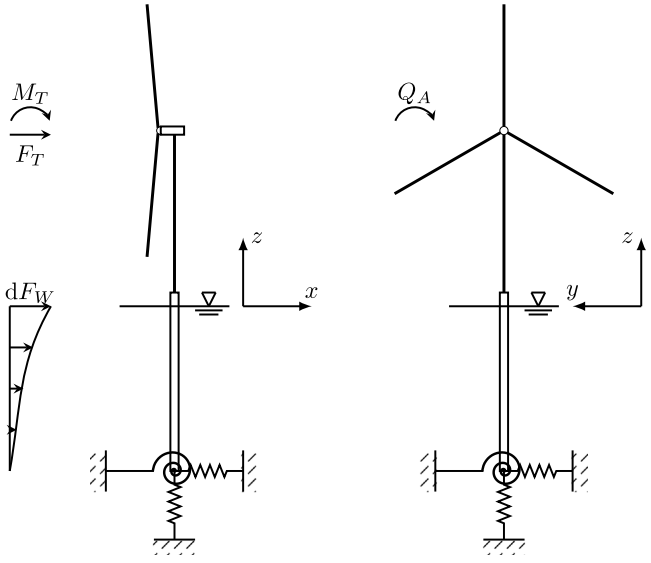

Fig. 4. Representation of the OWT simplified response model. The springs that represent the linear soil stiffness are placed at the mudline.

The structural response of the tower and monopile was found from modal superposition, where the first four fore-aft and side–side modes were considered. The total displacement at time t was found by multiplying the modal shape functions, ψ, by their corresponding

Table 3
Natural frequencies obtained by the linearized models for the three wind turbines.

Turbine model	NREL	DTU	IEA
1st fore-aft natural frequency	0.261 Hz	0.278 Hz	0.192 Hz

modal coordinates, χ (Eq. (1)). The modal coordinates were assumed harmonic, i.e. $\chi(t) = \chi_0 e^{i\omega t}$, and were found by solving the generalized equations of motion.

$$w(z,t) = \sum_{k=0}^{n} \psi_k(z)\chi_k(t) = \boldsymbol{\psi}(z)^\top \boldsymbol{\chi}(t). \tag{1}$$

The natural frequencies, summarized in Table 3, and the corresponding mode shapes of the models were determined by solving the eigenvalue problem for the 2D finite element beam model of the support structure with a rigid rotor. Using the principle of virtual work, the generalized system matrices can be established, as shown in detail by Hegseth and Bachynski (2019).

The wind turbine system is represented by a linear state–space model that consists of a structural part and a control part, which are coupled to obtain the complete closed-loop aero-hydro-servo-elastic model. The state variables include the position and velocity of the structure in modal coordinates, $\chi(t)$, and the rotor speed, $\dot{\varphi}$, which is described by a single degree of freedom drivetrain model, considering only the rigid body dynamics of the shaft (Eq. (2)).

$$I_D\,\ddot{\varphi} = Q_A - N_{gear}Q_G \tag{2}$$

Here, I_D is the drivetrain inertia, Q_A is the aerodynamic torque, N_{gear} is the gear ratio, and Q_G is the generator torque. The structural states can then be written in vector form as in Eq. (3).

$$\mathbf{x}_s = \begin{bmatrix}\boldsymbol{\chi}^\top & \dot{\boldsymbol{\chi}}^\top & \dot{\varphi}\end{bmatrix}^\top \tag{3}$$

The input variables of the structural system consist of the control actions, the wind, and wave input. The baseline linear control system follows the generic approach for variable-speed pitch-controlled wind turbines. It consists of a generator-torque controller and a collective blade-pitch controller, which are working independently in below-rated and above-rated wind speeds, respectively. For below-rated wind speeds, the generator torque is set to be proportional to the square of the rotor speed to maintain the optimal tip-speed ratio. For above-rated wind speeds, a gain-scheduled PI controller is used to modify the collective blade pitch angle to change the aerodynamic torque in order to follow the rated rotor speed. In both control regimes, the control system is described by a first order system, where the rotor speed, $\dot{\varphi}$, is the only input, and the outputs are the generator torque, Q_G, and the blade pitch angle, θ. The control inputs to the structural system are defined by Eq. (4).

$$\mathbf{u}_{sc} = \begin{bmatrix} Q_G \\ \theta \end{bmatrix} \tag{4}$$

Wind loads on the rotor were derived from linearized blade element momentum theory with the incoming wind field described by the Kaimal spectrum and an exponential coherence function in the longitudinal wind velocity component (IEC, 2019). The blades were considered rigid, and the aerodynamic forces on the rotor were applied as resultant loads at the tower top. The incoming wind was described by a rotor effective wind speed for each of the three resultant forces in Fig. 4, as described in detail by Hegseth et al. (2020), where F_T, M_T and Q_A represent the thrust, tilting moment and aerodynamic torque, respectively.

Wave loads were expressed by the load vector, $\mathbf{F}_W$, which contains the generalized wave excitation force for each degree of freedom. The hydrodynamic loads include first order wave loads from MacCamy–Fuchs theory, and viscous excitation based on stochastic linearization of the quadratic drag term in Morison's equation (Borgman, 1969). The wind-wave load vector is expressed by Eq. (5).

$$\mathbf{u}_{sd} = \begin{bmatrix} v_{F_T} & v_{M_T} & v_{Q_A} & \mathbf{F}_W^\top \end{bmatrix}^\top \tag{5}$$

Here, v_{F_T}, v_{M_T} and v_{Q_A} are rotor-effective wind speeds for thrust, tilting moment and aerodynamic torque, respectively.

The structural and control system models can be written as a single closed-loop system, where the structural states are related to control inputs and disturbances to forces. The equations of motion are then expressed in state–space form as

$$\dot{\mathbf{x}} = \mathbf{A}\mathbf{x} + \mathbf{B}\mathbf{u} \tag{6a}$$

$$\mathbf{y} = \mathbf{C}\mathbf{x} \tag{6b}$$

where $\mathbf{A}$ is the state matrix, $\mathbf{B}$ is the input, and $\mathbf{C}$ is set equal to the identity matrix. The closed-loop system is then transformed to the frequency domain, where the transfer matrix between input and output for a frequency ω is then defined by Eq. (7).

$$\mathbf{H}(\omega) = \mathbf{C}\,(i\omega\mathbf{I} - \mathbf{A})^{-1}\,\mathbf{B} \tag{7}$$

Assuming that the wind and wave excitation are uncorrelated (DNV-GL, 2016a), the cross spectral density matrix for the load processes, $\mathbf{S}_\mathbf{u}(\omega)$, can be written by Eq. (8), and the cross spectral density matrix of the output vector $\mathbf{y}$ for a frequency ω is calculated from Eq. (9).

$$\mathbf{S}_\mathbf{u}(\omega) = \begin{bmatrix} \mathbf{S}_{\text{wind}}(\omega) & \mathbf{0} \\ \mathbf{0} & \mathbf{S}_{\text{wave}}(\omega) \end{bmatrix}, \tag{8}$$

$$\mathbf{S}_\mathbf{y}(\omega) = \mathbf{H}(\omega)\mathbf{S}_\mathbf{u}(\omega)\mathbf{H}(\omega)^H \tag{9}$$

Here $(\cdot)^H$ denotes its conjugate transpose (Naess and Moan, 2012). The response spectra of $\mathbf{y}$ are then found along the diagonal of $\mathbf{S}_\mathbf{y}(\omega)$.

To evaluate the validity of the simplified models, the fore-aft bending moment spectra were compared to spectra from time domain simulations of the fully coupled models. Five 1-hr simulations were conducted for each load case and the resultant spectra were averaged. Fig. 5 shows an example of the comparisons for 10 MW and 15 MW models. Good agreement between the resulting stress spectra is observed. The simplified models have lower responses at the wave frequencies, due to their higher stiffness (linear-elastic) compared to the nonlinear stiffness of the macro-element used for the fully coupled models. In the natural frequency region, the responses are generally similar for operational conditions, while a higher sensitivity to the amount of the stiffness-proportional Rayleigh damping levels is observed for the parked conditions. This will be further discussed in Section 5.

2.3. Short-term damage calculation

Both time domain and frequency domain approaches can be used to calculate short-term fatigue damage. The following sections describe the details for each approach, as applied here.

2.3.1. Time domain

In time domain, the short-term fatigue damage is estimated from fully integrated time domain analyses considering turbulent wind and irregular waves, for a specified period (1 h) with stationary environmental conditions. Fatigue damage is determined from the time histories of axial stress σ_x, calculated from the axial forces and bending moments (Katsikogiannis et al., 2021), at various heights along the support structure, and positions around the circumference of the tower and monopile. Damage estimates are based on Palmgren–Miner's linear damage accumulation rule (DNV-GL, 2016b) and the use of characteristic S–N curves. Curves "D" for steel in seawater with cathodic protection, and for steel in air were selected for the monopile and tower, respectively (DNV-GL, 2020). A reference thickness equal to 25 mm

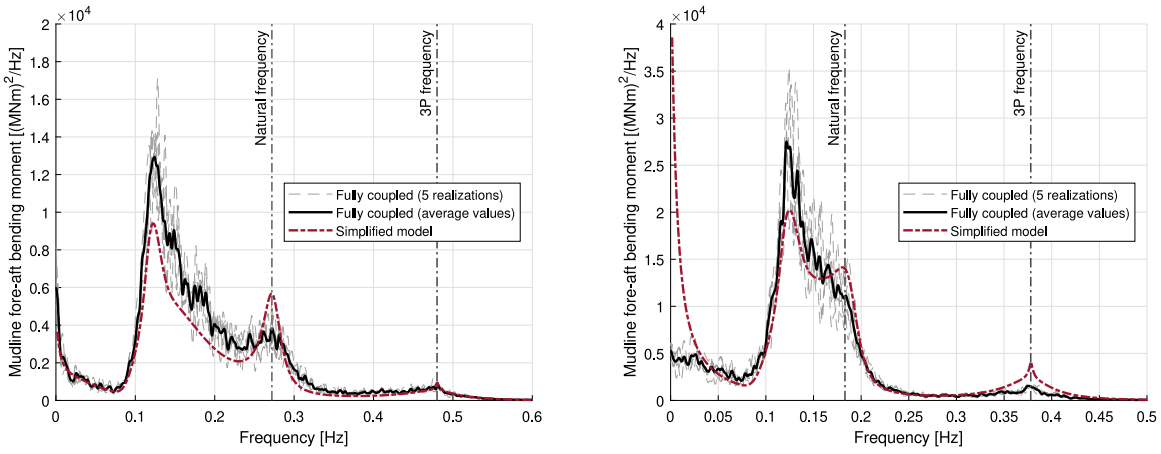

(a) $U_w = 21$ m/s, $H_s = 3.5$ m, $T_p = 8.3$ m/s (b) $U_w = 21$ m/s, $H_s = 3.4$ m, $T_p = 8.2$ m/s

Fig. 5. Comparison of mudline fore-aft bending moment spectra between simplified and fully coupled models. (a) 10 MW (b) 15 MW.

and a thickness exponent on fatigue strength of 0.2 were used (DNV-GL, 2020). No stress concentration factors were considered. The fatigue damage is estimated using the rainflow cycle counting method (Matsuishi and Endo, 1968) using the WAFO Toolbox (Brodtkorb et al., 2000), modified to allow for bi-linear S–N curves (Bachynski et al., 2014).

2.3.2. Frequency domain

In frequency domain, closed-form formulations based on stress spectra were used. Depending on the spectral bandwidth parameter $\beta = \sqrt{m_2^2/(m_0 \cdot m_4)}$, where m_i is the ith spectral moment of the stress spectrum, two different approaches were applied. Values of $\beta \geq 0.96$ indicate a narrow-banded spectrum (Barltrop and Adams, 1991), otherwise a wide-banded process is assumed. For a narrow-banded spectrum, the short-term stress ranges follow a Rayleigh distribution. Therefore, the total number of cycles can be expressed by the mean zero up-crossing rate, ν_0, and the short-term (1 h) fatigue damage for the environmental condition $H_{s,i} - T_{p,j}$ is calculated from Eq. (10) (Naess and Moan, 2012).

$$d^*(H_{s,i}, T_{p,j}) = 3600 \cdot \nu_0 \cdot \sigma_{eq}^m / K \tag{10}$$

Here, σ_{eq} is the equivalent stress range, which represents a constant stress range loading that is equivalent to the random loading, assuming a single slope S–N curve with fatigue strength exponent m, and a material fatigue parameter, K. For a narrow-banded Gaussian process with zero mean, σ_{eq} is calculated from Eq. (11) (Naess and Moan, 2012).

$$\sigma_{eq}^m = (2\sqrt{2m_0})^m \cdot \Gamma(1 + m/2) \tag{11}$$

Here, m_0 is the zeroth spectral moment representing the variance of stress spectrum of the sea state $H_{s,i} - T_{p,j}$, and $\Gamma(\cdot)$ is the Gamma function.

For a wide-banded process, several empirical solutions have been proposed such as Wirsching and Shehata (1977), Zhao and Baker (1992), Dirlik (1985), Tovo (2002), Benasciutti and Tovo (2005) and Gao and Moan (2008). The Dirlik empirical formulation is used here, which has been widely used for fatigue evaluation of offshore structures, giving accurate results over a wide range of bandwidths for a stationary Gaussian process (Gao and Moan, 2008). The Dirlik approach approximates the stress range distribution by using a combination of one exponential and two Rayleigh probability density functions (Dirlik, 1985; Hegseth and Bachynski, 2019; Mršnik et al., 2013).

The closed-form formulations require a single slope parameter m. From a full fatigue assessment, where bi-linear curves are used to calculate the damage, it was found that the main contributor to the total fatigue damage is the high cycle region, above 10^6 cycles. Fig. 6 shows

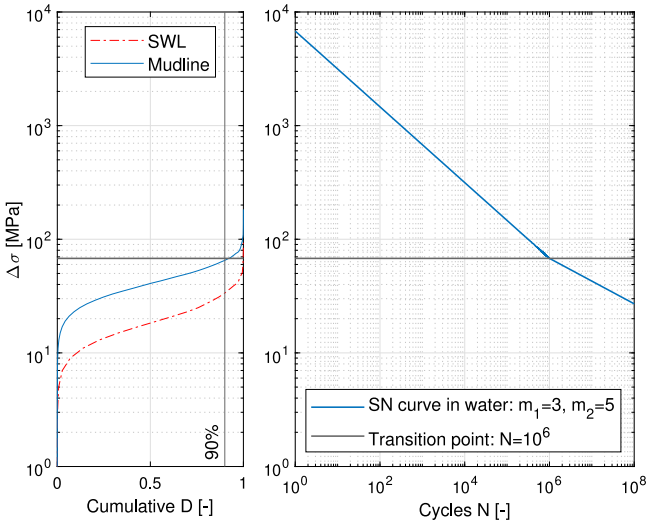

Fig. 6. Comparison of the total cumulative long-term fatigue damage and SN curve in water, from full scatter fatigue assessment (5 MW model).

the comparison of the cumulative fatigue damage for two locations along the 5 MW model, and the SN curve in seawater. Close to SWL, the fatigue damage occurs entirely in the high-cycle region, while close to and below the mudline, due to relatively larger responses, approximately 10% of the long-term damage is caused by stress ranges above the transition point. Similar results were found from the full fatigue assessment for the 10 MW and 15 MW models, therefore, a single value $m = 5$ is used in the closed-form formulations.

3. Damage-equivalent lumping method

This section describes the damage-equivalent lumping method and how it is applied using the fully coupled and simplified models. The method presented by Katsikogiannis et al. (2021) extracts the lumped load cases based on representative damage-equivalent contour lines, and it consists of two main steps. The first step is to derive the transfer functions and stress spectra along the support structure, for each $H_{s,i} - T_{p,j}$ combination in the wave scatter diagrams, using typical wave spectra. The second step is to determine the damage-equivalent contour lines, to obtain the lumped load cases. The application of the method using the fully coupled and simplified models differs only in the first step, e.g. in the derivation of the stress spectra.

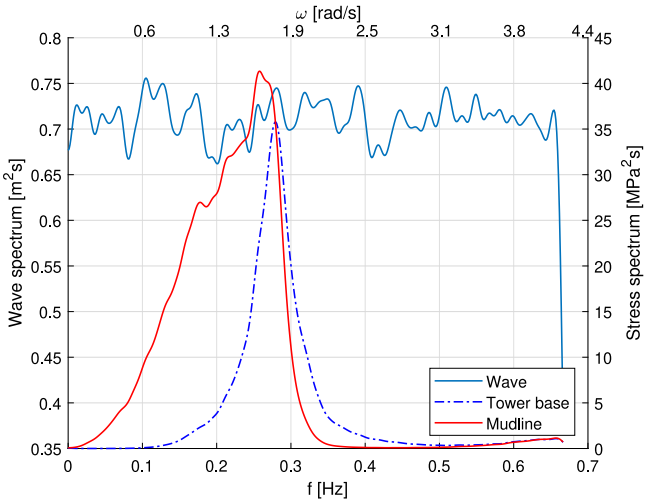

Fig. 7. White noise wave spectrum and corresponding stress spectra at mudline and tower base of the 10 MW OWT. Wind class 18–20 m/s (operational).

3.1. Derivation of stress spectrum using fully coupled models

When using fully-coupled models, for each wind class, the OWT model was subjected to a 3-hr white noise wave excitation and uniform wind. As a result, a linear stress transfer function, $H_{\zeta\sigma}$, relating wave elevation to stress response was extracted (Eq. (12)), for different positions along the support structure. Frequencies between 0 Hz and 0.7 Hz (4.4 rad/s) were considered, to include all relevant response frequencies.

$$S_{\sigma\sigma}(f,z) = H^2_{\zeta\sigma}(f,z) \cdot S_{\zeta\zeta}(f) \tag{12}$$

$S_{\sigma\sigma}(f,z)$ is the power spectral density of the stress response, $S_{\zeta\zeta}(f)$ is the incident white noise wave spectrum, and z is the vertical position along the OWT support structure.

The significant wave height of the white noise analysis was chosen as the mid value of the most probable H_s class of the wave scatter diagram associated with the wind class. The selection is based on the fact that for these types of structures, the most contributing sea states to the long-term fatigue damage are generally those with the largest probability of occurrence. Furthermore, the transfer functions shall be defined adequately over the entire frequency range in the scatter diagram, therefore MacCamy & Fuchs' load model (MacCamy R.C., 1954) was applied, to account for diffraction effects that become important for certain frequency ranges for increasing monopile diameter. Fig. 7 shows an example of the white noise wave spectrum with the stress spectra at mudline and tower base of the 10 MW model.

The spectral approach relates the wave input to the stress response, therefore, the response spectra should represent the OWT dynamic response caused only by wave loads. To capture the effect of aerodynamic damping and mean thrust, minimizing dynamic excitation by the wind, the operational turbine is subjected to a constant, uniform wind field. Tower shadow effects were disabled to avoid aerodynamic excitation interfering with the transfer functions. Furthermore, the inclusion of the mean thrust is also important for capturing the soil response. Specifically, the nonlinear deflection soil characteristics (stiffness, damping) of the macro-element model, are assumed linear to the slope representative of the deflection resulting from the mean responses to the aerodynamic thrust. The resulting non-zero mean value in the response is subtracted from the time series before computing the response spectrum.

3.2. Derivation of stress spectrum using simplified models

Contrary to the fully coupled model, where a 3-h white noise excitation with uniform wind was required, the stress spectra along the support structure for each $H_{s,i} - T_{p,j}$ combination were derived directly as an output from the linearized frequency domain model, further reducing the computational time in the lumping process.

3.3. Damage-equivalent contour lines

Having determined the stress spectra, three quantities are required to extract the contour lines for each location along the OWT. Firstly, the unit fatigue damage $d^*(H_{s,i}, T_{p,j})$ is calculated in the frequency domain (Section 2.3.2), which represents the short-term damage for a specified time period with stationary environmental conditions.

The second quantity that is required is the total long-term fatigue damage, $D_{LT,target}$: the target fatigue damage for a wave scatter diagram SD_k, representative of wind class k. Following Palmgren–Miner's linear damage accumulation hypothesis (ABS, 2014; DNV-GL, 2016b), the long-term damage of each sea state class in the wave scatter diagram, d_{LT}, is calculated by multiplying the unit damage (d^*) with the probability of occurrence of the sea state class and a specified number of years N_y (expressed in hours), according to Eq. (13). The target long-term fatigue damage, $D_{LT,target}$, is the summation of d_{LT} over the sea states in the wave scatter diagram (Eq. (14)).

$$d_{LT}(H_{s,i}, T_{p,j}) = N_y \cdot p(H_{s,i}, T_{p,j}) \cdot d^*(H_{s,i}, T_{p,j}) \tag{13}$$

$$D_{LT,target} = N_y \cdot \sum_{i=1}^{N_{H_s}} \sum_{j=1}^{N_{T_p}} p(H_{s,i}, T_{p,j}) \cdot d^*(H_{s,i}, T_{p,j}) \tag{14}$$

The third quantity is the scaled unit fatigue damage for a sea state, $D_{U,scale}$, which is based on the total probability of occurrence (p_k) of the wave scatter SD_k (Eq. (15)). $D_{U,scale}$, estimated based on Eq. (16), represents the long-term fatigue damage at a specified location, assuming that only the evaluated sea state class would occur in wave scatter SD_k.

$$p_k = \sum_{i=1}^{N_{H_s}} \sum_{j=1}^{N_{T_p}} p(H_{s,i}, T_{p,j}) \tag{15}$$

$$D_{U,scale} = N_y \cdot d^*(H_{s,i}, T_{p,j}) \cdot p_k \tag{16}$$

The damage-equivalent contour line for a specific location consists of all $H_{s,c} - T_{p,c}$ combinations for which the scaled 1-h fatigue damage $D_{U,scale}$ (Eq. (16)) is equal to the target long-term fatigue damage $D_{LT,target}$ (Eq. (14)), and can be expressed by the condition in Eq. (17).

$$N_y \cdot d^*(H_{s,c}, T_{p,c}) \cdot p_k = N_y \cdot \sum_{i=1}^{N_{H_s}} \sum_{j=1}^{N_{T_p}} p(H_{s,i}, T_{p,j}) \cdot d^*(H_{s,i}, T_{p,j}) \tag{17}$$

An example is shown in Fig. 8 for the wave scatter diagram of the wind class 16–18 m/s. Two locations along the support structure for the 10 MW OWT were considered, the mudline and the tower base (11.5 m above SWL). For three fixed H_s values, the scaled unit fatigue damage distribution over the peak periods is plotted, together with the target fatigue damage. The intersection points define the peak periods for which, for the specified H_s, the two damage quantities are equal. The scaled unit damage distribution as a function of wave period follows a curve similar to a dynamic amplification factor of a single-degree-of-freedom system. Specifically, for peak periods close to the first natural period (~ 4 s) resonance effects cause a steep increase of the fatigue damage. For long wave periods, the response is considered as quasi-static, decreasing the number of load cycles per time and the resulting fatigue damage. Similarly, for short wave periods, although the number of load cycles increases, the dynamic amplification tends to zero as high-frequency external force produces little response and

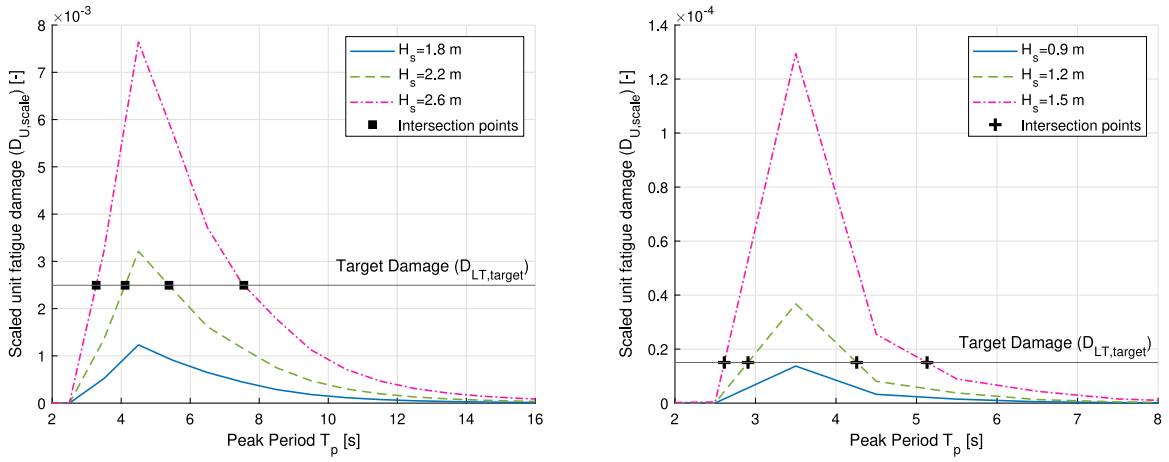

(a) Mudline (b) Tower base

Fig. 8. Scaled unit fatigue damage ($D_{U,scale}$) distribution for fixed H_s values and target long-term fatigue damage ($D_{LT,target}$) for mudline and tower base. Wind class 16–18 m/s.

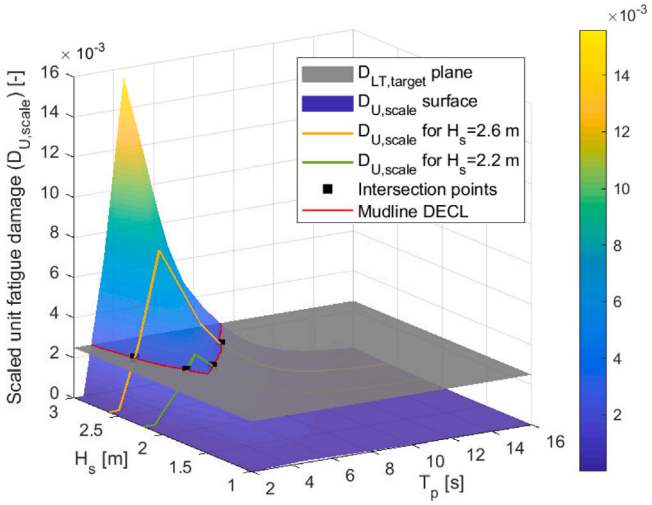

Fig. 9. Scaled unit fatigue damage (multi-coloured surface) for determining damage-equivalent contour line at mudline for wind class 16–18 m/s. (For interpretation of the references to colour in this figure legend, the reader is referred to the web version of this article.)

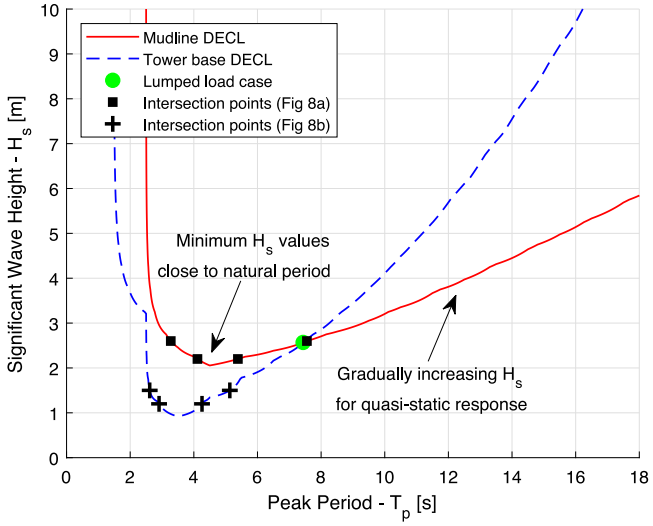

Fig. 10. Damage-equivalent contour lines at mudline-tower base for the 10 MW model and the resultant lumped load case for wind class 16–18 m/s. (For interpretation of the references to colour in this figure legend, the reader is referred to the web version of this article.)

therefore low fatigue damage. The scaled unit fatigue damage for all $H_s - T_p$ values within the scatter diagram forms a surface, where all the intersection points with $D_{LT,target}$ are defined. Those points form the contour line for a specified location along the OWT. An example of such surface is shown in Fig. 9 for the mudline, together with the target fatigue damage, represented by the grey plane. The $D_{U,scale}$ distribution for the fixed H_s values and intersection points from Fig. 8a are also plotted.

Fig. 10 shows the damage-equivalent contour lines at mudline and tower base for wind class 16–18 m/s. The intersection points for fixed H_s values from Fig. 8 are also plotted. These are $H_s - T_p$ combinations that satisfy the condition in Eq. (17) only for the specified location along the OWT. The green circle is the intersection point of the contours for which the equality in Eq. (17) is satisfied for both locations, representing the lumped sea state $H_{s,c} - T_{p,c}$. The shape of the contours reflects the dynamic behaviour of the structure (Katsikogiannis et al., 2021), similar to the fatigue damage distribution in Fig. 8. Additionally, the contour lines lie above a minimum H_s value (in the vicinity of the natural period), meaning that for lower values, there are not any peak periods so that the resultant sea state excites the structure to the desired $D_{LT,target}$ level. This was observed in Fig. 8, where for a range of H_s values, that include, e.g. $H_s = 1.5$ m for the mudline and $H_s = 0.8$ m for the tower base, the scaled unit fatigue damage does not intersect with the target damage. Finally, for a given H_s value, the target damage level can be achieved with two different peak periods, something that is reflected also in Fig. 8. Only the upper T_p values were considered as potential lumped load cases in the study. The lumped sea states, each one representative of a wind class scatter diagram, make up the reduced load set for fully-integrated time domain analyses for fatigue damage calculation.

4. Long-term fatigue damage calculation

4.1. Full long-term fatigue assessment

For the full fatigue assessment, for each sea state $H_{s,i} - T_{p,j}$ in a wave scatter diagram SD_k associated with wind class k, the unit fatigue damage, $d^*_{1h}(H_{s,i}, T_{p,j})$, was calculated. The long-term damage is then calculated as the sum of the short-term damage of each sea state, scaled by the probability of occurrence $p(H_{s,i}, T_{p,j})$, from Eq. (18).

The total fatigue damage is calculated as the summation over the wind classes, k. Four approaches have been used to determine the long-term fatigue damage and their accuracy and computational time were compared (Table 4).

$$D_{LT,k}^{flt} = N_y \cdot \sum_{i=1}^{N_{H_s}} \sum_{j=1}^{N_{T_p}} p(H_{s,i}, T_{p,j}) \cdot d_{1h}^{*}(H_{s,i}, T_{p,j}) \tag{18}$$

4.1.1. Fully coupled models

Using the fully coupled models, the OWTs were subjected to 1 h (IEC, 2019; DNV-GL, 2016b) time domain simulation with simultaneous turbulent wind and irregular waves for each $H_{s,i} - T_{p,j}$. Then, $d_{1h}^{*}(H_{s,i}, T_{p,j})$ is calculated based on rainflow counting (Section 2.3.1). This method, denoted as TD LTFA, (used as a reference for comparisons) is the most computationally demanding, requiring approximately 1009 time domain simulations for each OWT.

4.1.2. Simplified models

The second approach, denoted as FD LTFA uses the simplified model for the full long-term fatigue assessment. For each $H_{s,i} - T_{p,j}$ combination, $d_{1h}^{*}(H_{s,i}, T_{p,j})$ is calculated in frequency domain (Section 2.3.2), and the long-term damage is calculated from Eq. (18). This approach is the most efficient, reducing 99% the computational effort.

4.2. Lumping method using the fully coupled and simplified models

The damage-equivalent lumping method was applied using the fully coupled (LMFC) and simplified models (LMSM), and the lumped load cases were obtained for each wind class. Then, the load cases were analysed using 1-h time domain simulations and the short-term damage is calculated. Due to the increased statistical uncertainty when a single sea state represents a scatter diagram (Katsikogiannis et al., 2021), five stochastic realizations with random wind and wave seeds were conducted for each load case, as a compromise between accuracy and computational effort. For a lumped load case $H_{s,l} - T_{p,l}$ that represents a scatter diagram SD_k with probability of occurrence p_k, the long-term fatigue damage is calculated from Eq. (19).

$$D_{LT,k}^{lumped} = N_y \cdot d_{1h}^{*}(H_{s,l}, T_{p,l}) \cdot p_k \tag{19}$$

Applying the lumping method using the fully coupled models reduces approximately 90% the computational time compared to TD LTFA, considering the 3-hr white noise and the 5 1-hr time domain simulations for each wind class. The use of the simplified model in the lumping process further reduces the computational time (95%) as the white noise simulations are not required. Table 4 shows the four approaches to determine the long-term fatigue damage, and summarizes them in terms of accuracy and computational time compared to the time domain full long-term fatigue assessment (TD LTFA). The results are further discussed in Section 5.3.

Table 4
Summary of methods used for long-term fatigue assessment. The accuracy and computational time are compared to TD LTFA.

Method	Lumping	Damage calculation	Computational time	Accuracy
1 - TD LTFA	N/A	Fully coupled	1	–
2 - FD LTFA	N/A	Simplified	0.005	~50%
3 - LMFC	Fully coupled	Fully coupled	0.1	~95%
4 - LMSM	Simplified	Fully coupled	0.04	~95%

5. Results and discussion

5.1. Lumped load cases for various locations along OWT

The contribution from quasi-static and dynamic loads varies along the OWT, resulting in different target and scaled unit fatigue damage along the support structure. An example is shown in Fig. 11a, where the scaled unit fatigue damage is plotted as a function of peak period for a given H_s value, for different locations along the support structure (10 MW model). Maximum values were found below mudline, and close to the natural period of the structure, as expected. Similarly, Fig. 11b shows how the target long-term fatigue damage varies along the monopile.

For the tower, the response is mainly dominated by the acceleration of the rotor-nacelle assembly, and the damage-equivalent contour lines (DECLs) were almost identical for all locations (Katsikogiannis et al., 2021). For the monopile, dynamic loads due to waves become increasingly important for locations deeper along the structure due to the large moment arm, leading to variations of the DECLs especially for large peak periods. Therefore, the extracted lumped load cases from the DECLs vary depending on the locations along the support structure that are used.

Fig. 12 shows an example of DECLs for the 10 MW model at the tower base, and various locations along the monopile, together with the extracted lumped cases for all the locations considered. For all wind classes, a small difference of the $H_s - T_p$ values was observed, as shown in the zoomed part of Fig. 12, caused by the slight variations of the DECLs along the monopile. For most of the wind classes, the differences for H_s were between 0.04 m - 0.1 m, and 0.05 s - 0.2 s for T_p. Similar

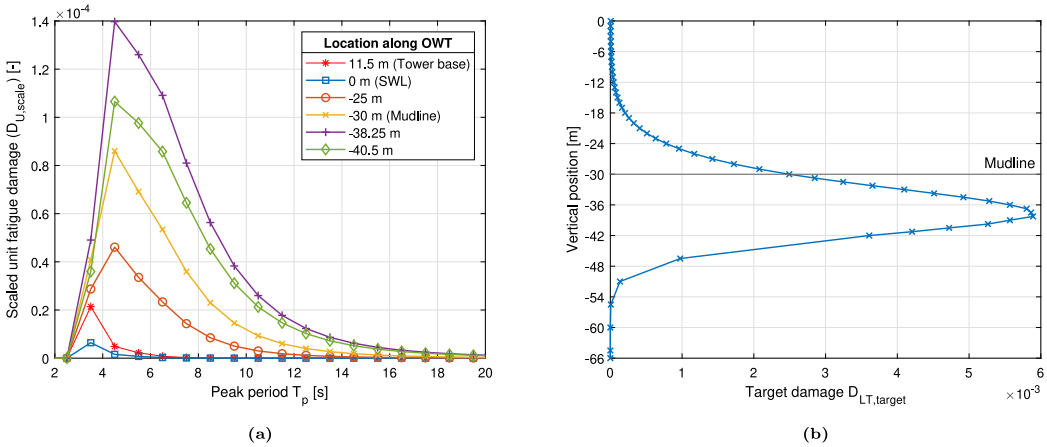

Fig. 11. (a) Scaled unit fatigue damage ($D_{U,scale}$) as a function of peak period for a given H_s, for various locations along OWT. (b) Target long-term fatigue damage ($D_{LT,target}$) along monopile. 10 MW OWT model.

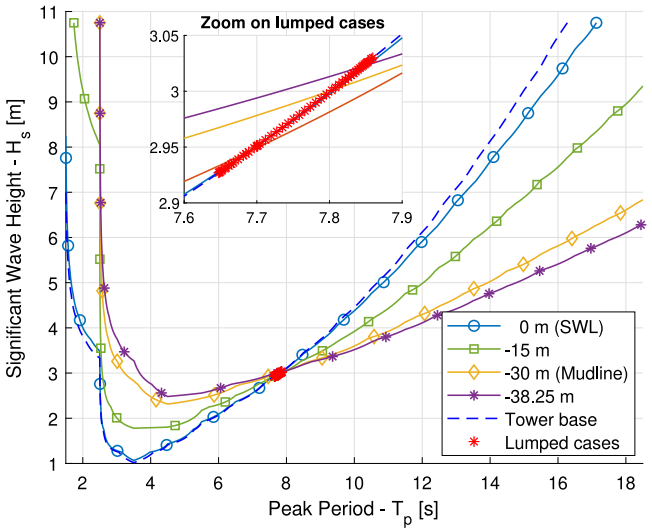

Fig. 12. DECLs for tower base and different locations along the monopile. Red markers indicate the resulting lumped load cases using tower base DECL and DECLs from all locations along the monopile. 10 MW OWT. (For interpretation of the references to colour in this figure legend, the reader is referred to the web version of this article.)

variations were also observed for the 5 MW, and 15 MW models. For locations close to SWL, the dynamic response of the monopile is similar to the tower base, leading to similar DECLs as it can be seen in Fig. 12.

For support structures similar to the ones here, the lumped load cases can be extracted from two locations with sufficient distance, to avoid similarity in the DECLs. One should be representative of the tower response (e.g. tower base), and one of the monopile responses, preferably at the lower part (e.g. mudline), to adequately capture the dynamic response due to wave loads. The exact location chosen is of little influence as the $H_s - T_p$ variations can be considered negligible compared to the statistical uncertainty in the fatigue damage estimation.

5.2. Lumping method applied to 5-10-15 MW OWTs

5.2.1. Damage-equivalent contour lines

The damage-equivalent lumping method was applied to the fully coupled and simplified models. 13 wind classes were considered with step 2 m/s between 4–30 m/s, using the wind speed at the hub height for each OWT. The wind classes are represented by OWT-specific wave scatter diagrams due to the difference in the hub height between the models. For each OWT model, the representative damage-equivalent contour lines (DECL) for each wind class were extracted from the tower base and the mudline.

Fig. 13 shows the contour lines, and stress transfer functions, for wind class 18–20 m/s, for the three models at the tower base and mudline. The shape of the contour lines has an inverse relationship to the stress transfer functions. In the vicinity of the natural period, due to resonance, small values of H_s are required to excite the structure to the target damage level, and a local minimum is observed. With increasing period, the stress transfer functions gradually decrease, depicting low

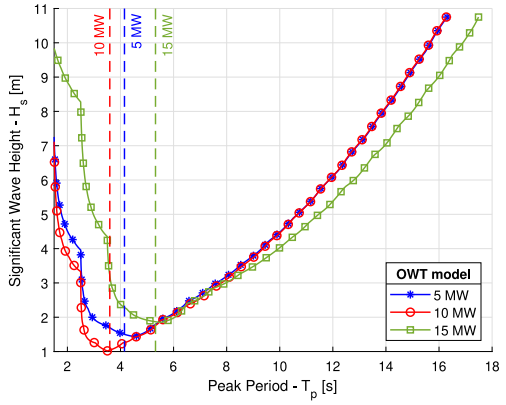

(a) Tower base contour lines

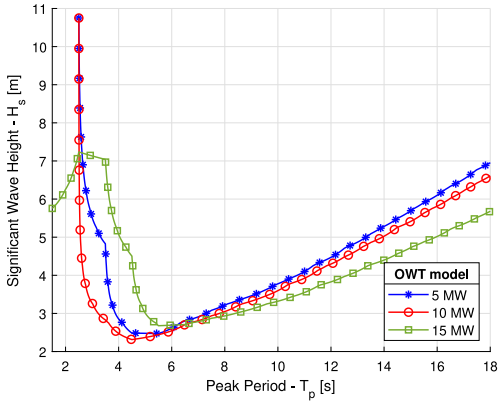

(b) Mudline contour lines

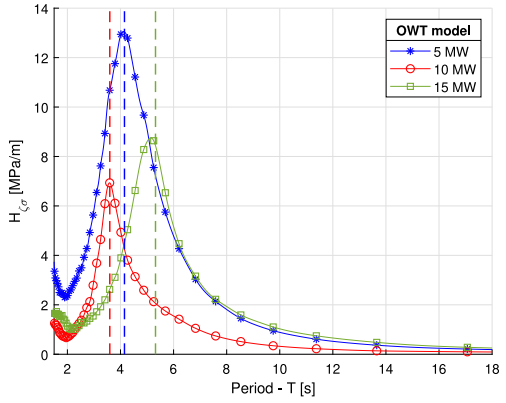

(c) Tower base stress transfer function

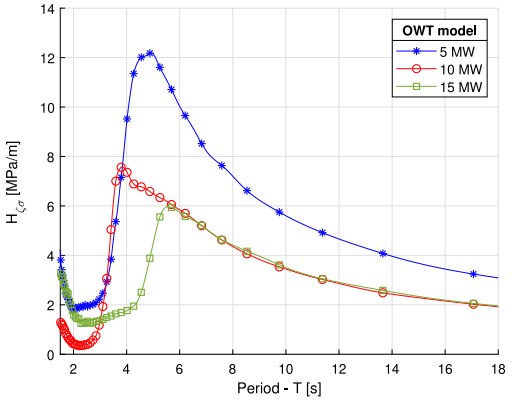

(d) Mudline stress transfer function

Fig. 13. Damage-equivalent contour lines (DECLs) and stress transfer at functions at tower base and mudline for the three OWT models. Wind class 18–20 m/s.

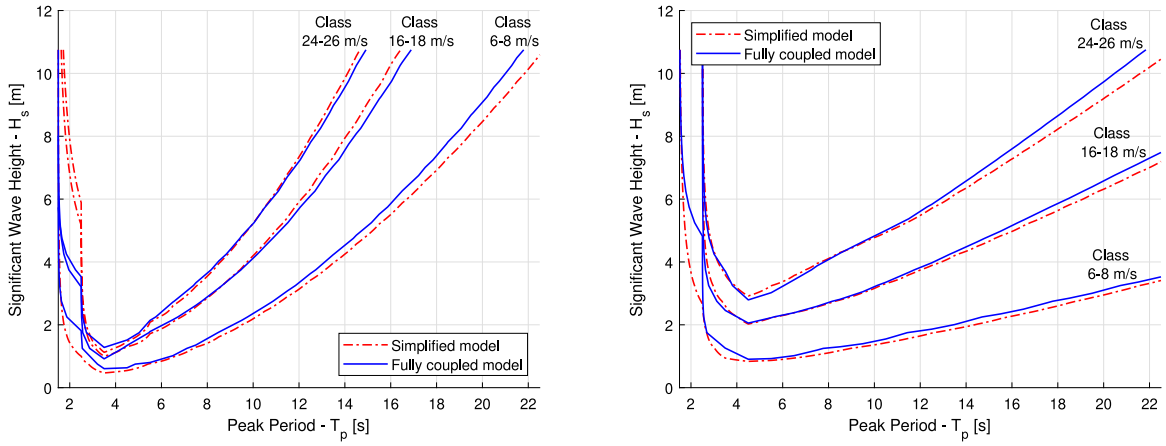

(a) Tower base (b) Mudline

Fig. 14. Contour lines from the simplified and the fully coupled models at the tower base and mudline for three wind speed classes. 10 MW offshore wind turbine.

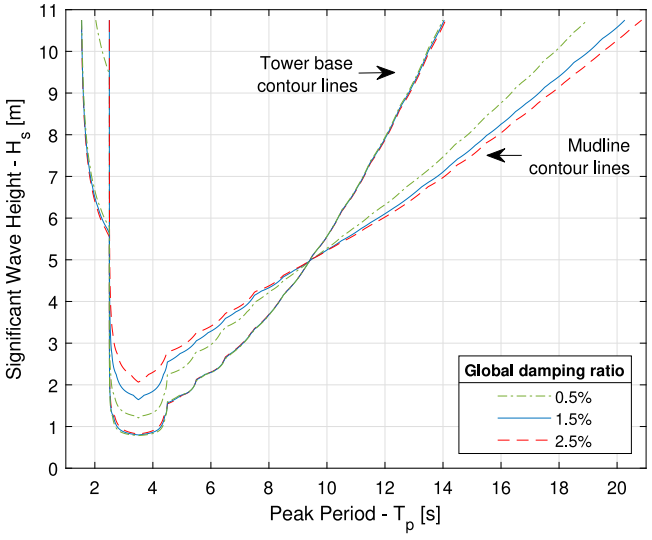

Fig. 15. Influence of amount of global damping ratio applied to the simplified model on the resulting contour lines for wind class 26–28 m/s (parked).

dynamic response, leading to a gradual increase of the H_s values along the contour lines. The differences in the natural frequencies between the three models (Fig. 3), are clearly reflected in the contour lines, where the local minimum of the H_s values for the 5 MW and 10 MW models is observed slightly higher and lower than 4 s respectively, while for the 15 MW, it is found approximately at 5.5 s.

Fig. 14 shows a comparison of the contour lines, as obtained from the simplified and the fully coupled models for the 10 MW OWT for different wind classes. A good agreement was observed, as the contour lines from the simplified models follow the same trend, capturing the response characteristics of the wind turbines both in the vicinity of the natural period and for larger periods, where they behave quasi-statically.

The contour lines from the simplified models were sensitive to the control system parameters, e.g. gain scheduling parameters. The amount of stiffness-proportional Rayleigh damping was only important for the parked conditions, mainly close to the natural frequency, without affecting the resulting lumped load cases. An example is shown is Fig. 15 for three different damping levels for wind class 26–28 m/s. Negligible effects from Rayleigh damping were observed for the operational conditions, or for the tower base in general.

5.2.2. Lumped load cases

The intersection between the contour lines at the tower base and mudline forms the representative lumped load case. Fig. 16 shows the lumped load cases for the three OWT models for all wind classes, as obtained from the fully coupled models.

Similar H_s values are found for the three models, increasing gradually from low to high wind speeds. The differences in the H_s values between the models come solely from the different distribution of the sea states in the wind class scatter diagrams, which are based on the hub height wind speed (calculated using the power law from the 10 m wind speed) at 90 m (5 MW), 119 m (10 MW), or 150 m (15 MW). Therefore, the same wind speed at lower hub height is associated with more severe sea states, something that is reflected in the representative scatter diagrams. This explains the increasing H_s values from the 15 MW to the 5 MW model, especially for higher wind speeds.

The peak period of the lumped load cases is influenced by two effects. Firstly, for intermediate and high wind classes, the higher H_s values, which result from the more severe sea states in the scatter diagrams, are associated with higher T_p values. This results in slightly larger T_p values for the 5 MW model compared to the 10 MW and 15 MW models. For the lower wind classes, the dynamic properties of the OWTs seem to have a stronger influence on the resultant T_p values for the lumped load cases, with the 15 MW model having about 1 s larger peak period. This difference comes from the higher (around 1.5 s) natural period of the 15 MW model, which also affects how the unit scaled damage is distributed over the periods.

Fig. 17 shows the H_s, T_p values of the lumped load cases from the fully coupled and the simplified models, for the three OWTs. For both sea state parameters there is a strong agreement between the obtained values for the models, for all OWTs. For all wind classes, the H_s values obtained from the simplified models were similar to those from the fully-coupled models, with the differences being found between 0.05 m (4%) to 0.2 m (16%). Similarly, the T_p values varied between 0.1 s (2%) to 0.4 s (8%), compared to values obtained from the fully coupled models. The largest differences were found for the wind classes close to rated speed, mainly for the 15 MW model. However, those differences did not affect notably the long-term fatigue damage results, as shown in Section 5.3.

5.3. Long-term fatigue damage comparisons

This section evaluates the accuracy of the fatigue damage from the lumped load cases (LMFC & LMSM) and the simplified model (FD LTFA), compared to results from the time domain long-term fatigue assessment (TD LTFA). Details for the long-term damage calculations

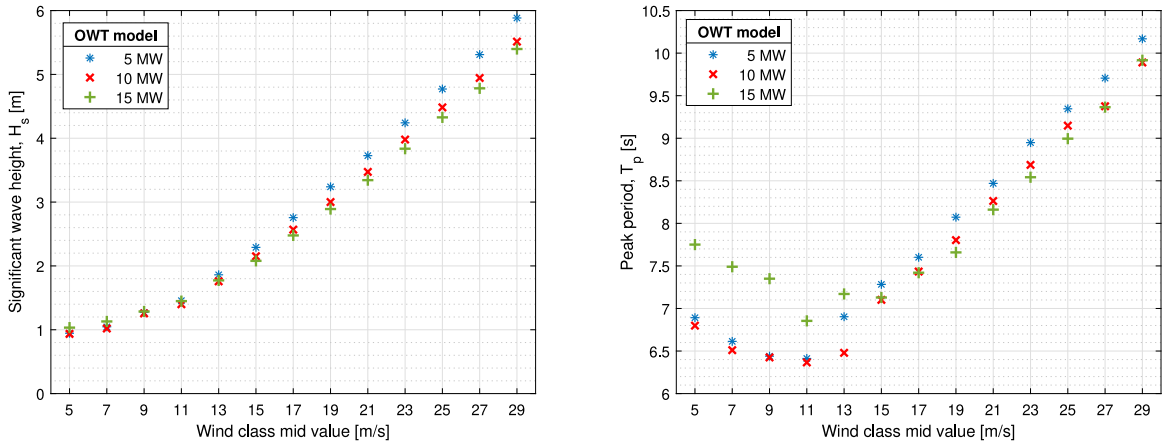

(a) Lumped H_s (b) Lumped T_p

Fig. 16. Lumped load cases for the three OWT models.

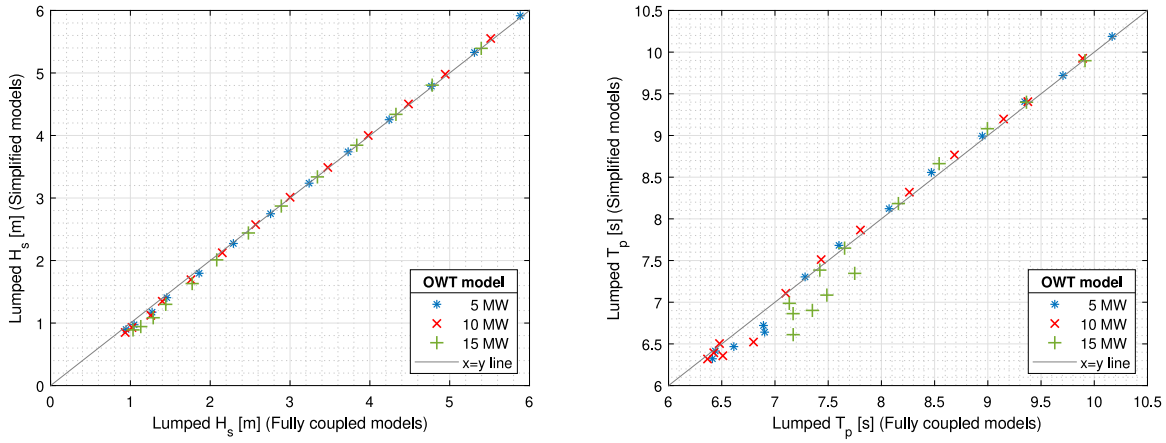

(a) Lumped H_s (b) Lumped T_p

Fig. 17. Comparison of $H_s - T_p$ values of the lumped load cases, as obtained from the fully coupled and the simplified models.

are given in Section 4. Fig. 18 shows the long-term fatigue damage comparisons at mudline for each wind class. The results are discussed in detail in the following sections.

5.3.1. Long-term fatigue damage from lumped load cases (LMFC & LMSM)

For the lumped load cases, each bar in Fig. 18 shows the mean long-term fatigue damage from the five time domain realizations, while the error bars indicate the standard deviation. The lumped load cases generally predict the fatigue damage well for individual wind classes. For the operational wind speed classes, the relative differences with respect to full scatter results for all models mostly varied between ±15%, with a few cases reaching up to ±30%. Those differences are within the level of stochastic variability in the time domain realizations, indicated by the error bars. Similar accuracy was observed for the damage estimates at the tower base (not shown), with slightly higher stochastic variation, mainly for wind classes close to the rated speed. The slightly different lumped load cases from LMFC & LMSM methods, did not affect the accuracy of the method, leading to variations within the range of the stochastic variability.

For the parked states (26–30 m/s), in addition to the seed variability, damage estimates were sensitive to the chosen wave kinematics model, which becomes increasingly important due to the lack of aerodynamic damping. It should be noted that the selection of the wave kinematics model for the lumped load cases is based on Table 2. From the time domain long-term fatigue assessment, it was found that the sea states that were modelled with 2nd order waves (Table 2) contributed to the long-term damage between 30% to 50% (26–28 m/s), and 40% to 70% (28–30 m/s), depending on the OWT. This poses a challenge for the selection of wave kinematics for the lumped load cases, as Airy theory tends to underestimate the damage estimates, while 2nd order waves tend to overestimate them. The sensitivity of the dynamic response in shown in Fig. 19, which shows the mudline response spectra of the lumped load case of 28–30 m/s class of the 10 MW OWT, choosing Airy and 2nd order wave kinematics. The plots are the average of 5 time domain realizations with the same wind and wave seeds.

The total fatigue damage relative difference between lumped load cases (LMFC) and time-domain long-term fatigue assessment (TD LTFA) for the three OWT models is shown in Fig. 20. The results from the lumped load cases obtained using simplified models (LMSM) are nearly identical to LMFC, and therefore are not shown. The results are compared at the tower base, mudline, and at the OWT location with the maximum fatigue damage. The angular position of the maximum damage around the circumference is considered. A negative (positive) difference implies an underestimation (overestimation) of the damage calculated by the lumped load cases. Below and at the mudline, the relative difference of the long-term fatigue damage varies between −6% to + 1%, while for the tower base, the variations are slightly higher, ranging between ±10%. Considering all the relevant uncertainties related to the lumping process, fatigue calculation, and nonlinearities, the deviations for the total fatigue damage are small, especially in view of the ∼95% reduction of the computational time for the three models.

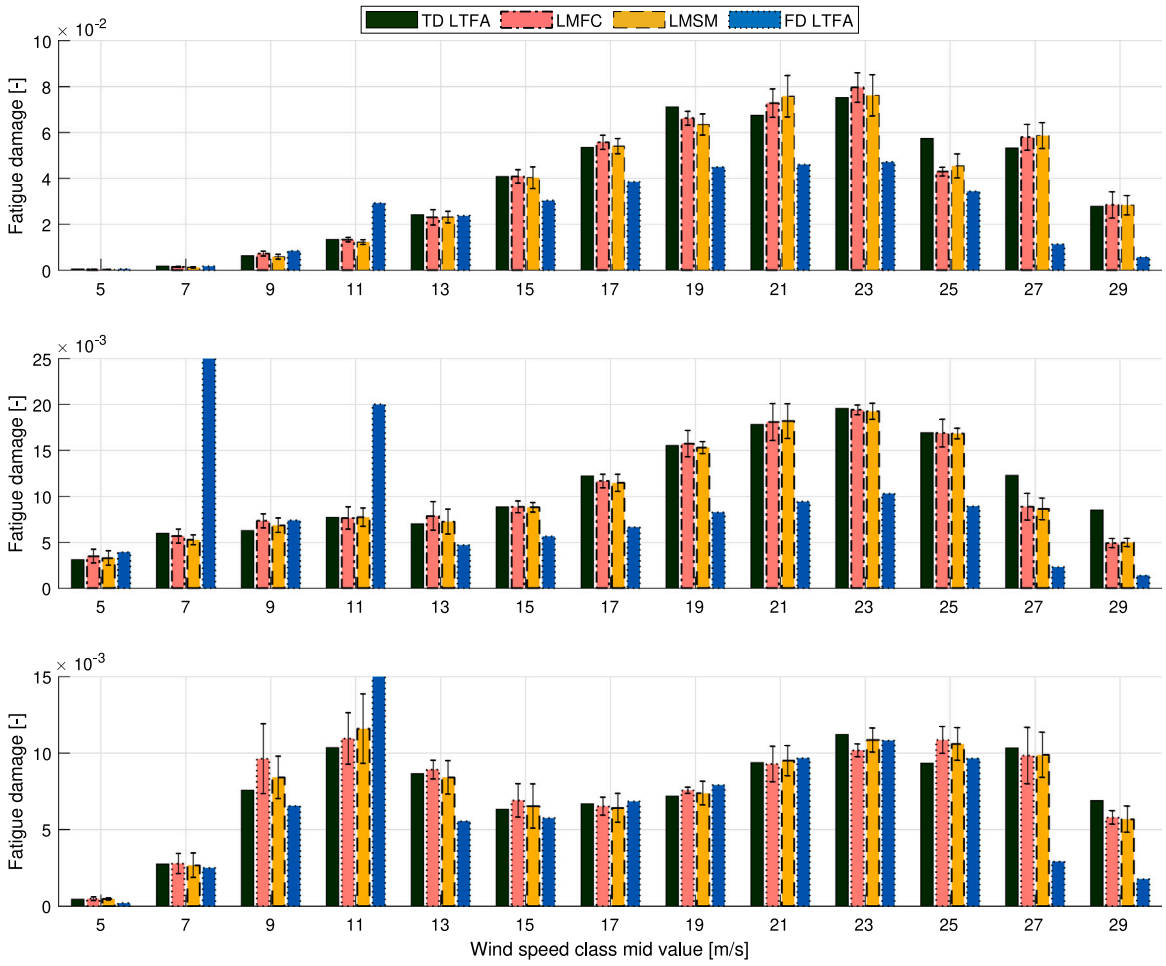

Fig. 18. Contribution of individual wind speed classes to total long-term fatigue damage for the three OWTs at mudline. Comparison between time domain (TD LTFA) and frequency domain long term fatigue assessment (FD LTFA), and lumped load cases obtained using fully coupled (LMFC) and simplified models (LMSM). Error bars on top of lumped cases indicate the standard deviation from the time domain realizations. Top: 5 MW — Middle: 10 MW — Bottom: 15 MW. Note that for the classes 7 m/s (10 MW) and 11 m/s (15 MW) the bars extend beyond the *y*-axis limit, and the figure was cut for visual purposes.

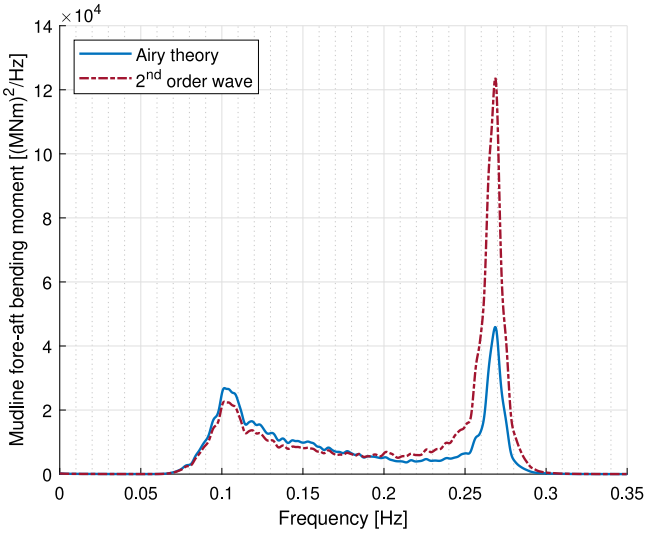

Fig. 19. Response spectra of the lumped load case of 10 MW OWT, for wind class 28–30 m/s, using Airy and 2nd order wave kinematics.

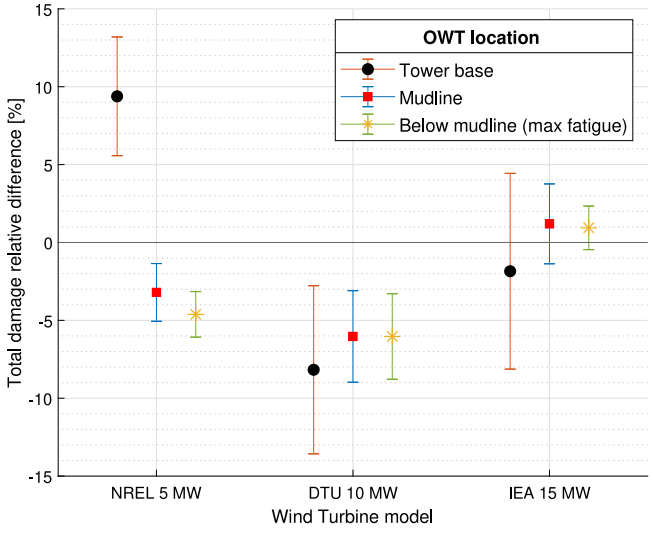

Fig. 20. Total fatigue damage relative difference between lumped load cases (LMFC) and time-domain long-term fatigue assessment (TD LTFA) for the three OWT models. Comparison at the location of the maximum damage around the circumference.

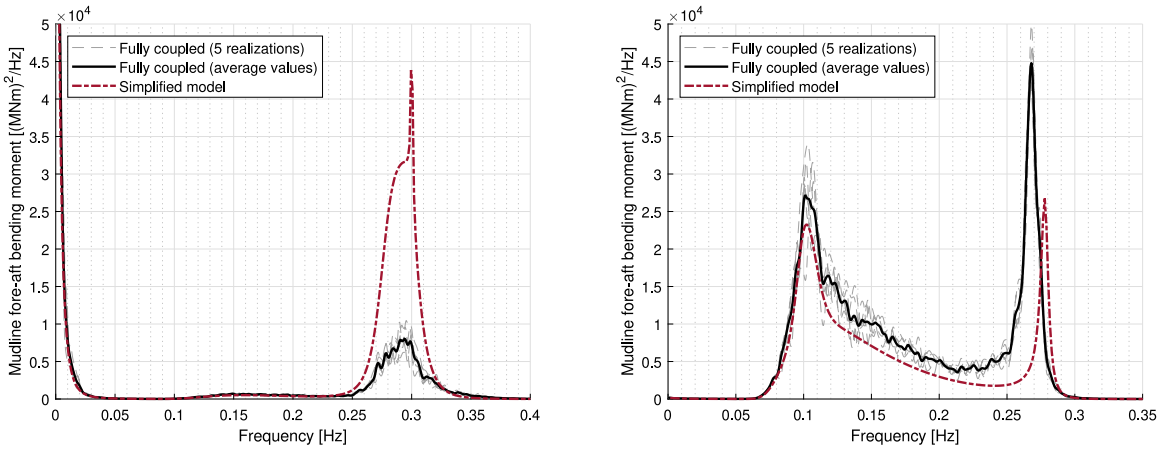

(a) 6-8 m/s wind class - 10 MW OWT

(b) 28-30 m/s wind class - 10 MW OWT

Fig. 21. Comparison of mudline bending moment spectra between fully coupled and simplified models.

5.3.2. *Long-term fatigue damage from simplified model (FD LTFA)*

The simplified model captures the dynamic response of the OWTs, the FD LTFA captures most trends in the long-term fatigue damage distribution from different wind classes. However, for most cases, the FD LTFA leads to discrepancies compared to time domain results.

For the operational cases below and above rated speed, the fatigue damage was underpredicted mostly between 20% to 50% for the 5 MW and the 10 MW models, and between 3% to 10% for the 15 MW model. The differences mainly come from the higher stiffness provided by the simplified model, which results in lower responses in the wave frequency range. For those classes, the responses around the natural frequency were in good agreement between the models for all OWTs, indicating that the total damping (aerodynamic, structural, soil, hydrodynamic) is sufficiently represented in the simplified model. The "better" accuracy in the fatigue damage for the 15 MW model is caused mostly by the simplified model overpredicting the low frequency response and the response at the 3P excitation frequency. The aforementioned effects are also visible in Fig. 5, where the mudline response spectra between the fully coupled and the simplified models are compared. At the rated speed, the simplified model overpredicted the fatigue damage for all turbines due to considerably higher responses at very low frequencies. For that particular wind class, the nonlinear behaviour of control system is significant, and it cannot be accurately captured by the simplified model. A special case is observed for wind class 7 m/s, for the 10 MW model. As shown in Fig. 21a this is caused by a significant overprediction of the response close to 3P/1st fore-aft bending mode resulting in unreasonably large damage estimates for the simplified model (~0.056).

For the parked conditions, the simplified model underestimates the damage by 70% to 80% for all turbines. For those conditions, the responses in the vicinity of the natural frequency dominate the fatigue damage, and soil damping is the main source of damping. The stiffness-proportional Rayleigh damping for each OWT was tuned so the global damping is approximately 1.3% (Section 2.2.2), to approximate the damping level of the macro-element model for mid-load values. However, for the parked conditions, where the mean thrust force is negligible, the global damping ratio of the fully coupled models is between 0.6% to 1%, as found from the decay tests (Fig. 3). The simplified model is thus more damped than the time domain model, which reduces the dynamic response at the natural frequency, as shown in Fig. 21b. The higher stiffness of the simplified model is also evident in Fig. 21b through the slight increase of the natural frequency and reduced response in the main wave frequency range.

6. Conclusion

Different approaches for fatigue assessment of monopile-based offshore wind turbines have been considered. Fully coupled, nonlinear time domain models, and simplified frequency domain models were used both for direct long-term fatigue assessment and in combination with a damage-equivalent contour line method. The accuracy and computational effort were compared to full long-term time domain fatigue assessment (TD LTFA). The NREL 5 MW, DTU 10 MW, and IEA 15 MW reference wind turbines were used.

Firstly, a lumping method based on damage-equivalent contour lines approach was applied using fully coupled (LMFC) and simplified models (LMSM). The method condenses each wave scatter diagram associated with a wind speed class to a single lumped load case. Selected lumped load cases were subjected to simultaneous wind-wave loads in time domain simulations to predict long-term fatigue damage. For the fully coupled models, the method extracts stress spectra from 3-hr white-noise wave excitation and uniform wind, for each wave scatter diagram. For the simplified models, the stress spectra are derived directly as an output from the simplified model. Damage-equivalent contour lines are defined along the support structure, and their intersection is considered the representative lumped sea state.

The simplified models were able to accurately capture the dynamic characteristics of the OWTs. The lumping method using fully coupled and simplified models resulted in similar contour lines and lumped load cases, with their variations being negligible compared to the uncertainty in the time domain fatigue damage estimation. Two locations along the support structure were sufficient for the extraction of the lumped load cases, as long as these could adequately represent the dynamic response of the tower and the monopile. Additionally, for the simplified models, variations in the amount of damping did not affect the resulting lumped load cases.

The accuracy of the damage estimates from the lumping method mostly varied ±15% for individual wind speed classes, for all turbines. For the parked conditions, the chosen wave kinematics model had a notable effect on the damage estimates, mainly for the tower base, due to the lack of aerodynamic damping. The total fatigue damage estimates had an accuracy of 92%–98% along the support structure for all OWTs. Applying the lumping method using fully coupled and simplified models, the computational time was reduced by 90% and 96% respectively, compared to full long term time domain fatigue assessment.

The simplified model was also used for a full long term frequency domain fatigue assessment (FD LTFA). This method was the most computationally efficient (99.5% reduction), however it resulted in discrepancies up to 80% compared to time domain assessment. Variations

were mainly due to the linear soil stiffness, which resulted in lower responses in wave frequency excitation, sensitivity to damping (mainly for parked conditions), and the simplified representation of the control system, which becomes particularly important below and at rated wind speed.

The damage-equivalent lumping method had similar accuracy for turbines with different characteristics, and can be recommended to practitioners for fatigue design purposes, and sensitivity studies. Further research is recommended to evaluate the applicability of the method for different type of support structures (e.g. gravity-based structures, jackets). Given that simplified models of reasonable accuracy are available, they can be used to extract the lumped load cases, and then combined with fully coupled time domain models to estimate damage, providing the best combination of accuracy and computational effort.

CRediT authorship contribution statement

George Katsikogiannis: Conceptualization, Methodology, Validation, Formal analysis, Data curation, Writing – original draft, Writing – review & editing, Visualization. **John Marius Hegseth:** Conceptualization, Methodology, Validation. **Erin E. Bachynski-Polić:** Conceptualization, Validation, Writing – review & editing, Supervision, Project administration, Funding acquisition.

Declaration of competing interest

The authors declare that they have no known competing financial interests or personal relationships that could have appeared to influence the work reported in this paper.

Acknowledgements

The authors gratefully acknowledge the support from the Wave Loads and Soil Support for Extra Large Monopiles (WAS-XL) project (NFR grant 268182). Additionally, part of this work has been carried out in the framework of RedWin 2 project (REDucing cost of offshore WINd), NFR grant 296511.

References

Aarnes, O.J., Breivik, Ø., Reistad, M., 2012. Wave extremes in the northeast atlantic. J. Clim. 25 (5), 1529–1543. http://dx.doi.org/10.1175/JCLI-D-11-00132.1.

ABS, 2014. Guide for The Fatigue Assessment Of Offshore Structures. American Bureau of Shipping, Houston, TX 77060 USA.

Bachynski, E.E., Kvittem, M.I., Luan, C., Moan, T., 2014. Wind-wave misalignment effects on floating wind turbines: Motions and tower load effects. J. Offshore Mech. Arct. Eng. (ISSN: 0892-7219) 136, http://dx.doi.org/10.1115/1.4028028.

Bachynski, E., Ormberg, H., 2015. Comparison of engineering models for the aerodynamic load distribution along a wind turbine blade. In: Proceedings of the Twenty-Fifth International Ocean and Polar Engineering Conference - ISOPE 2015. 2015, pp. 561–567.

Bak, C., Zahle, F., Bitsche, R., Kim, T., Yde, A., Henriksen, L.C., Natarajan, A., Hansen, M.H., 2013. Description of the DTU 10 MW Reference Wind Turbine. Report, DTU Wind Energy, Kgs. Lyngby, DK.

Barltrop, N.D.P., Adams, A.J., 1991. Dynamics of Fixed Marine Structures (Third Edition), third ed. Butterworth-Heinemann, Oxford, ISBN: 978-0-7506-1046-9, pp. 613–616. http://dx.doi.org/10.1016/B978-0-7506-1046-9.50017-1.

Benasciutti, D., Tovo, R., 2005. Spectral methods for lifetime prediction under wide-band stationary random processes. Int. J. Fatigue 27 (8), 867–877. http://dx.doi.org/10.1016/j.ijfatigue.2004.10.007, Cumulative Fatigue Damage Conference - University of Seville 2003.

Borgman, L.E., 1969. Ocean wave simulation for engineering design. Journal of the Waterways and Harbors Division 95 (4), 557–586. http://dx.doi.org/10.1061/JWHEAU.0000665.

Brodtkorb, P., Johannesson, P., Lindgren, G., Rychlik, I., Ryden, J., Sjo, E., 2000. WAFO—A MATLAB Toolbox for the analysis of random waves and loads. In: 10th International Offshore and Polar Engineering Conference (ISOPE), Vol. 3. pp. 343–350.

Bruserud, K., Haver, S., 2016. Comparison of wave and current measurements to NORA10 and NoNoCur hindcast data in the northern north sea. Ocean Dyn. 66 (6–7), 823–838. http://dx.doi.org/10.1007/s10236-016-0953-z.

Burton, T., Jenkins, N., Sharpe, D., Bossanyi, E., 2011. Wind Energy Handbook. John Wiley & Sons, Ltd, ISBN: 9781119992714, http://dx.doi.org/10.1002/9781119992714.

Correia, A., 2011. A Pile-head Macro-element Approach to Seismic Design of monoshaft supported bridges (Ph.D. thesis). European School for Advanced Studies in Reduction of Seismic Risk, ROSE School, Pavia, Italy.

Dirlik, T., 1985. Application of Computers in Fatigue Analysis (Ph.D. thesis). University of Warwick, URL http://wrap.warwick.ac.uk/2949/.

DNV-GL, 2016a. Loads and site conditions for wind turbines. Det Norske Veritas, DNVGL-ST-0437.

DNV-GL, 2016b. Support structures for wind turbines. Det Norske Veritas, DNVGL-ST-0126.

DNV-GL, 2017a. Environmental conditions and environmental loads. Det Norske Veritas, DNVGL-RP-C205.

DNV-GL, 2017b. Riser fatigue. Det Norske Veritas, DNVGL-RP-F204.

DNV-GL, 2020. Fatigue design of offshore steel structures. Det Norske Veritas, DNVGL-RP-C203.

Du, J., Chang, A., Wang, S., Li, H., 2014. A novel lumping block method for fatigue damage assessment of mooring chain. In: Proceedings of the International Offshore and Polar Engineering Conference. pp. 366–372.

Gaertner, E., Rinker, J., Sethuraman, L., Zahle, F., Anderson, B., Barter, G., Abbas, N., Meng, F., Bortolotti, P., Skrzypinski, W., Scott, G., Feil, R., Bredmose, H., Dykes, K., Sheilds, M., Allen, C., Viselli, A., 2020. Definition of the IEA 15-Megawatt Offshore Reference Wind Turbine. Tech. Rep., International Energy Agency, Denver, CO, US, URL https://www.nrel.gov/docs/fy20osti/75698.pdf.

Gao, Z., Moan, T., 2008. Frequency-domain fatigue analysis of wide-band stationary Gaussian processes using a trimodal spectral formulation. Int. J. Fatigue 30, 1944–1955. http://dx.doi.org/10.1016/j.ijfatigue.2008.01.008.

Hegseth, J.M., Bachynski, E.E., 2019. A semi-analytical frequency domain model for efficient design evaluation of spar floating wind turbines. Mar. Struct. 64, 186–210. http://dx.doi.org/10.1016/j.marstruc.2018.10.015.

Hegseth, J.M., Bachynski, E.E., Martins, J.R.R.A., 2020. Integrated design optimization of spar floating wind turbines. Mar. Struct. 72, http://dx.doi.org/10.1016/j.marstruc.2020.102771.

Hou, H.-M., Dong, G.-H., Xu, T.-J., 2019. An improved lumping block equivalent method for predicting fatigue damage of mooring system for fish cage. Ocean Eng. 193, 106567. http://dx.doi.org/10.1016/j.oceaneng.2019.106567.

IEC, 2019. Design requirements of offshore wind turbines. International Electrotechnical Commission (IEC) 61400-3.

Jia, J., 2008. An efficient nonlinear dynamic approach for calculating wave induced fatigue damage of offshore structures and its industrial applications for lifetime extension. Appl. Ocean Res. 30 (3), 189–198. http://dx.doi.org/10.1016/j.apor.2008.09.003.

Jonkman, B.J., 2009. TurbSim User's Guide: Version 1.50. Technical Report, Tech. Rep., National Renewable Energy Lab (NREL), http://dx.doi.org/10.2172/965520.

Jonkman, J., Butterfield, S., Musial, W., Scott, G., 2009. Definition of a 5MW Reference Wind Turbine for Offshore System Development. Report, National Renewable Energy Laboratory (NREL), Denver, CO, US, http://dx.doi.org/10.2172/947422.

Katsikogiannis, G., Sørum, S.H., Bachynski, E.E., Amdahl, J., 2021. Environmental lumping for efficient fatigue assessment of large-diameter monopile wind turbines. Mar. Struct. 77, 102939. http://dx.doi.org/10.1016/j.marstruc.2021.102939.

Kühn, M., 2001. Dynamics and Design Optimisation of Offshore Wind Energy Conversion Systems [Dissertation]. Technische Universiteit Delft, The Netherlands.

Low, Y.M., Cheung, S.H., 2012. On the long-term fatigue assessment of mooring and riser systems. Ocean Eng. 53, 60–71. http://dx.doi.org/10.1016/j.oceaneng.2012.06.017.

MacCamy R.C., F.R.A., 1954. Wave forces on piles: A diffraction theory. Office of Naval Research, U. S. Department of the Navy.

Matsuishi, M., Endo, T., 1968. Fatigue of metals subjected to varying stress. Proc. Kyushu Branch Japan Society of Mechanical Engineering 37–40.

Mittendorf, K., 2009. Joint description methods of wind and waves for the design of offshore wind turbines. Marine Technology Society Journal 43, 23–33. http://dx.doi.org/10.4031/MTSJ.43.3.2.

Mršnik, M., Slavič, J., Boltežar, M., 2013. Frequency-domain methods for a vibration-fatigue-life estimation – application to real data. Int. J. Fatigue 47, 8–17. http://dx.doi.org/10.1016/j.ijfatigue.2012.07.005.

Naess, A., Moan, T., 2012. Stochastic Dynamics of Marine Structures. Cambridge University Press, http://dx.doi.org/10.1017/CBO9781139021364.

Page, A., Grimstad, G., Eiksund, G., Jostad, H.P., 2018. A macro-element pile foundation model for integrated analyses of monopile based offshore wind turbines. Ocean Eng. Vol. 167, 23–35. http://dx.doi.org/10.1016/j.oceaneng.2018.08.019.

Page, A., Grimstad, G., Eiksund, G., Jostad, H.P., 2019. A macro-element model for multidirectional cyclic lateral loading of monopiles in clay. Comput. Geotech. Vol. 106, 314–326. http://dx.doi.org/10.1016/j.compgeo.2018.11.007.

Page, A., Skau, K.S., Jostad, H.P., Eiksund, G., 2017. A new foundation model for integrated analyses of monopile-based offshore wind turbines. Energy Procedia Vol. 137, 100–107. http://dx.doi.org/10.1016/j.egypro.2017.10.337.

Passon, P., 2015. Damage equivalent wind-wave correlations on basis of damage contour lines for the fatigue design of offshore wind turbines. Renew. Energy Vol. 81, 723–736. http://dx.doi.org/10.1016/j.renene.2015.03.070.

Passon, P., Branner, K., 2014. Condensation of long-term wave climates for the fatigue design of hydrodynamically sensitive offshore wind turbine support structures. Ships Offshore Struct. 11, 142–166. http://dx.doi.org/10.1080/17445302.2014.967994.

Reistad, M., Breivik, O., Haakenstad, H., Aarnes, O.J., Furevik, B.R., Bidlot, J.-R., 2011. A high-resolution hindcast of wind and waves for the north sea, the norwegian sea, and the barents sea. J. Geophys. Res. Oceans 116 (C5), http://dx.doi.org/10.1029/2010JC006402.

2017. RIFLEX 4.10.3 User Guide. Tech. Rep., SINTEF Ocean.

Seidel, M., 2014a. Wave induced fatigue loads - insights from frequency domain calculations. Stahlbau 83 (8), 535–541. http://dx.doi.org/10.1002/stab.201410184.

Seidel, M., 2014b. Wave induced fatigue loads on monopiles - new approaches for lumping of scatter tables and site specific interpolation of fatigue loads. In: International Wind Engineering Conference (IWEC).

Sheehan, J.M., Grealish, F.W., Harte, A.M., Smith, R.J., 2005. Characterizing the wave environment in the fatigue analysis of flexible risers. J. Offshore Mech. Arct. Eng. 128 (2), 108–118. http://dx.doi.org/10.1115/1.2185129.

2017. SIMO 4.10.3 User Guide. Tech. Rep., SINTEF Ocean.

Song, X., Du, J., Wang, S., Li, H., Chang, A., 2016. An innovative block partition and equivalence method of the wave scatter diagram for offshore structural fatigue assessment. Appl. Ocean Res. 60, 12–28. http://dx.doi.org/10.1016/j.apor.2016.08.005.

Song, X., Wang, S., 2019. A novel spectral moments equivalence based lumping block method for efficient estimation of offshore structural fatigue damage. Int. J. Fatigue 118, 162–175. http://dx.doi.org/10.1016/j.ijfatigue.2018.09.016.

Tovo, R., 2002. Cycle distribution and fatigue damage under broad-band random loading. Int. J. Fatigue 24 (11), 1137–1147. http://dx.doi.org/10.1016/S0142-1123(02)00032-4.

Wirsching, P.H., Shehata, A.M., 1977. Fatigue under wide band random stresses using the rain-flow method. Journal of Engineering Materials and Technology 99 (3), 205–211. http://dx.doi.org/10.1115/1.3443520.

Zhao, W., Baker, M.J., 1992. On the probability density function of rainflow stress range for stationary Gaussian processes. Int. J. Fatigue 14 (2), 121–135. http://dx.doi.org/10.1016/0142-1123(92)90088-T.